Oxidation induced crack closure in a nickel base superalloy: a novel phenomenon and mechanism assessed via combination of 2D and 3D characterization

Yuanguo Tan[a], Nong Gao[a], Philippa Reed[a]

a Department of Mechanical Engineering, Faculty of Engineering and Physical Sciences, University of Southampton, Southampton, SO17 1BJ, UK

Abstract

Understanding the mechanism of oxidation induced crack closure (OICC) is of great importance in understanding the fatigue resistance of materials operating at intermediate or high temperatures subjected to oxidation. Current work reveals that the occurrence of OICC is most closely related to the test frequencies and temperatures rather than the microstructure in a directionally solidified (DS) superalloy. Characterization techniques in three dimensions - X-ray scanning tomography (CT) and two dimensions - scanning electron microscopy (SEM) with attached energy-dispersive Xray spectroscopy (EDX) are combined to capture the oxides formed within the crack wake. These data are then incorporated into modified models to provide quantitative measurements of oxidation induced crack closure. Both the experimental and modelling results show that the external oxides forming close to the crack tip, result in a high crack tip opening displacement and thereby significant crack closure.

Key Words: superalloys, high-temperature fatigue, oxidation-induced crack closure, X-ray scanning tomography, crack-tip blunting

1. Introduction

Nickel base (Ni-based) superalloys are generally designed to serve in core parts of modern jet turbine engines and power generation turbomachinery, experiencing extremely high operating temperatures and complex stress states [1, 2]. Thus, the alloys are required to possess exceptional mechanical properties, not only high strength at high temperatures, but also excellent resistance to the coupled damage evolution of oxidation, fatigue and creep. Oxidation-related fatigue damage has recently incurred significant research interest [3-7], as it becomes the dominant factor limiting the fatigue life in some industry applications. In addition, the temperatures needed for jet propulsion and power generation are required to increase markedly to achieve higher fuel efficiency and tighter emission economies. Understanding the mechanism of oxygen-related fatigue behaviour is becoming a priority, as it may allow considerable safe fatigue lifetime extension for applications of Ni-based superalloys at high temperatures.

It is well recognized that the fatigue crack propagation (FCP) rate is accelerated by orders of magnitude under dwell loading and air conditions, due to the so-called environmentally-assisted cracking in polycrystalline superalloys [8-10]. The prevalent mechanisms are (1) stress assisted grain boundary oxidation (SAGBO) and (2) dynamic embrittlement (DE). The difference between the two theories is that the fast intergranular cracking is caused by (1) the formation and cracking of brittle oxides at the grain boundaries (GBs) or (2) the decohesion of GBs due to elemental oxygen migration [11-13]. Oxygen distribution ahead of the crack tip is characterized using techniques with high spatial resolution, such as transmission electron microscopy with attached energy dispersive X-ray spectroscopy (TEM-EDX) [14], secondary ion mass spectrometry (SIMS) [10, 15] and atom probe tomography [8]. Although the precise mechanism is still contentious, increasing numbers of recent studies reveal that several oxidation layers are indeed formed even in an extremely tiny (nano-scale) volume at GBs or at the interface between γ and primary γ' ahead of the crack.

In addition to the prevalent SAGBO and DE mechanisms, another oxygen-related fatigue mechanism is sometimes considered for single crystal (SX) superalloys: oxidation induced crack closure (OICC). It was initially proposed between 1970s and 1980s [16-19], as the near-threshold crack growth was found to be greatly decelerated in the air/moisture conditions, compared to vacuum conditions. Oxides with comparable thickness to crack opening displacement (COD) were thought to form within cracks, wedging cracks open, hence reducing the effective stress intensity range factor (ΔK_{eff}) and crack propagation rate. Further studies found that OICC process might be also related to test frequencies, as the crack propagation threshold is increased at lower frequency tests in single crystal (SX) superalloys [20]. More interestingly, the OICC process is thought to compete with DE process in a fatigue study of CMSX-6 and SRR99 SX superalloys tested at intermediate temperatures (500 ℃) [20]. A two-way slope of the $da/dN - \Delta K$ curve is found, as the OICC is inferred to occur in the low-ΔK regime, while DE happened in the high-ΔK regime. Although an OICC process may of significance due to its potential benefit in improving crack propagation resistance, detailed knowledge of this mechanism is very limited. Suresh and Louat et. al [16, 21] proposed two

models to quantitively assess OICC in the 1990s, considering the geometry relationship between the fatigue crack and oxides. Suresh's model could correlate the crack closure effects with the oxides' thickness and position within the crack wake. Nevertheless, they used oxides measured from the fracture surface to validate the model. This might cause an overestimation of the crack closure effects, as the oxides' thicknesses are formed both in the near-threshold regime and non-near-threshold regime. Henceforth, no more models were developed, partly due to the difficulty in validating the OICC models by using experimental data. Therefore, characterizing the OICC process appropriately is a considerable challenge, which may only occur in the near-threshold regime for fatigue tests (when a load shedding routine is typically followed to determine the crack growth threshold value).

In the current work, oxygen-affected fatigue behaviour is studied in a directionally solidified superalloy (CM247LC), in which the interplay between oxygen and fatigue crack propagation behaviour may be quite complicated. As mentioned, the OICC process is more often observed in single crystal alloys, while the SAGBO and DE processes are closely associated with the GBs in polycrystalline superalloys. The DS materials possess microstructural features of single crystal and polycrystalline superalloys, as the large columnar grains facilitate crack growth behaviour similar to that seen in single crystal superalloys [22], while the (few) GBs can allow for SAGBO or DE processes to occur. To understand the mechanisms in depth in such a DS material, systematic fatigue tests are designed and characterization approaches in two and three dimensions [22] have been employed to link the micro mechanisms to the macro fatigue crack propagation behaviours.

2. Experimental methods

The material used in the present work is directionally solidified (DS) CM247LC superalloy, provided by GE power. The chemical composition is listed in Table 1, and the heat treatment process is listed in previous research [22].

Table 1 Composition of CM247LC alloy (in wt.%)

Cr	Co	Al	Ti	W	Mo	Ta	Hf	C	Zr	B	Ni
8.25	9.23	5.31	0.75	9.50	0.51	3.20	1.46	0.75	<0.02	<0.02	Bal

2.1 Normal Long fatigue crack tests

Long fatigue crack tests were conducted on single edge notched bend bars (SENB) using an Instron 8501 servo-hydraulic testing machine with a high temperature testing rig at 650 ℃ and 725 ℃. The set-up of the tests is shown in Fig. 1 (a). The dimensions of the samples are 55 mm in length, 10 mm in width and breadth, respectively. A notch with a depth of 2.5 mm was machined by electrostatic discharge machining at the middle of the bend bar, acting as the stress concentrator to initiate a crack during the fatigue tests. The crack length was monitored via the direct current potential drop (DCPD) method. Current was provided via the wires spot welded at the end of the specimen. The potential drop caused by the crack growth could be obtained from the wires spot welded across the notch, while two more wires were placed away from the notch to normalize the data against temperature and current variations. The fatigue

crack length could be derived from the potential drop values measured using the secant method, and a calibration check was made by post-test crack measurement by comparing the calibrated crack length with benchmarks on the surface. Four high-intensity quartz lamps were used to heat the specimen. The temperature was monitored and controlled to an indicated $\pm$ 1 ℃ by a Eurotherm 815 thermal controller and R-type (platinum + 13% rhodium/platinum) thermocouples spot welded to the front side surface of the specimen. Two types of samples are designed for the tests: (1) where columnar grains are aligned with the loading direction which is denoted as an L sample (2) where columnar grains are aligned perpendicular to the loading direction which is denoted as T sample, as shown in Fig. 1 (b). Both L and T samples were tested at 650 ℃ and 725 ℃, in air, 0.1 load ratio, with 10 Hz sine waveform and 1 s – 1 s/90 s – 1 s – 1 s trapezoidal waveforms. The 1 s – 1 s/90 s – 1 s – 1 s trapezoidal loading waveform denotes 1 s segments for loading, 1 s/90 s for dwelling at the maximum load, 1 s for unloading, and 1 s dwelling at the minimum load.

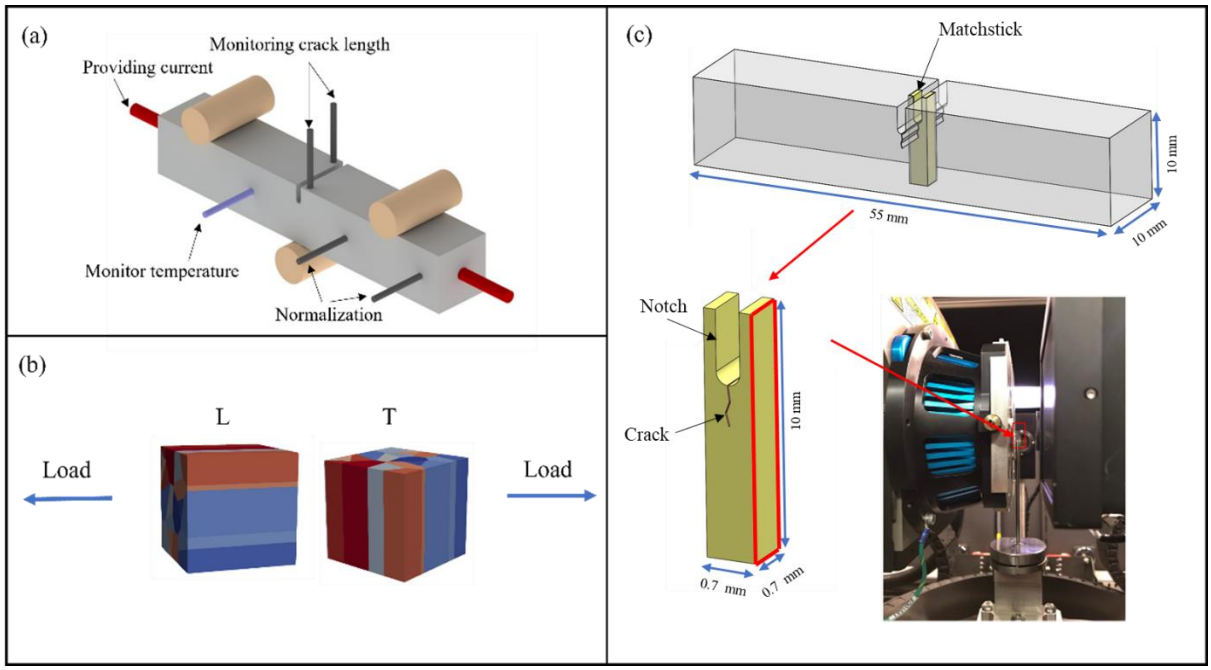

Figs. 1 schematic diagrams of (a) the set-up of the high-temperature fatigue test; (b) relationship between columnar grains and loading direction for two types of samples; (c) the matchstick sample and set-up of the Xray CT scanning.

Pre-cracking was conducted at the test temperature of interest, using a load shedding method with a sine waveform with a frequency of 10 Hz, a stress ratio of 0.1, and an initial ΔK of 20 MPa$\sqrt{m}$ after samples were stabilized at test temperature for 10 minutes. The ΔK was stepped down in 10% increments after the crack had grown through four monotonic plastic zone sizes at a constant ΔK maintained to within ±2% by load control variation until $\Delta K \approx 15$ MPa$\sqrt{m}$ was achieved, which ensured that crack growth out would occur from a microscopically sharp crack away from any residual effects induced in the machining of the notch. Then the loading waveform could then be changed to trapezoidal waveform (depending on the test frequency) with an initial ΔK of 15 MPa$\sqrt{m}$ under a constant load range (so increasing ΔK as the crack grew) until specimen failure.

2.2 Arrested and interrupted long fatigue crack tests

Arrested long fatigue tests: fatigue cracks could completely arrest under specific test conditions (which are detailed in the results), and two different methods were then used to force the crack growth to continue. One is increasing the stress intensity factor range (ΔK) by 10% through increasing the applied load range. The other one is denoted as 'crack-tip resharpening' which means changing the test frequency back to the 10 Hz sinewave form until the crack grows at this high-frequency loading condition until ΔK is increased by ~10% (by crack growth rather than changing the applied load), then transferring back to the desired test frequency. However, in some cases, the two methods have to be combined, because neither increasing stress intensity factor range by load increase nor crack-tip resharpening at higher frequency could force crack growth.

Interrupted long fatigue tests: three long fatigue crack tests which had arrested were interrupted to analyse the crack tips. One L sample was interrupted after being tested for 48 hours under a 1-1-1-1 trapezoidal waveform at 650 ℃. Another two interrupted tests were performed for T samples, one of which was interrupted after a 12-hour test under the 1-90-1-1 waveform, 650 ℃. Compared with the interrupted L test, this test experienced an almost equal accumulated overall dwell time at maximum load. The other T sample was interrupted after being tested for 96 hours under the 1-90-1-1 waveform, 650 ℃. No detectable crack growth was determined by the PD system during all the interrupted tests. All the tests are summarised in Table 2.

Table 2 Summary of the fatigue tests

	10 Hz sine waveform	1-1-1-1 waveform	1-90-1-1 waveform
650 ℃	1*L normal 1*T normal	1*L arrested 2*L interrupted 2*T normal	1*L arrested 1*T arrested; 1*T interrupted
725 ℃	1*L normal 1*T normal	1*L arrested 1*T arrested	1*L arrested 1*T arrested

2.3 SEM Analysis

A JEOL JSM 7200F field emission gun (FEG) SEM was employed for microstructure, fractography and crack tip morphology observation (imaging parameters are shown in Table 3). The cubic samples with dimensions of 10 mm × 10 mm × 10 mm were cut from the heat-treated block, and then grinded, polished and etched for microstructure analysis. The grinding, polishing and etching process are described in [22]. The chemical composition of the crack tips was analysed using Energy Dispersive Xray Spectrometer (EDX) attached to the SEM with accelerated voltage of 15 KeV, 10 μA current, 1 μm step size and 10 s dwell time.

Table 3 Imaging parameters in JEOL SEM JSM 7200F

Imaging mode	Acceleration voltage	Probe current	Imaging time	Working distance
SEI	15 kV	8 mA	20 s	9.9 mm

2.4 X-ray computed tomography (Xray CT)

X-ray CT was employed to evaluate the 3D morphology of the crack (particularly the crack tip). Due to the high X-ray attenuation of nickel, a 'matchstick' specimen of 0.7 × 0.7 × 10 mm^3 was extracted from the L and T tested coupons interrupted after being tested for 48 and 96 hours under 1-1-1-1 and 1-90-1-1 trapezoidal waveform at 650 ℃ shown in Figs. 1 (c). To generate the matchstick, a sample with dimensions of approximately 1.5 × 1.5 × 10 mm^3 was firstly cut out before being carefully ground down to the desired dimensions of 0.7 × 0.7 × 10 mm^3. The sample was scanned via Xradia Versa CT scanner with parameters shown in Table 4. The comparatively lower voxel resolution scanning is used for capturing the microstructure features, the whole crack morphology and obtaining the coordinates of the crack tip (region of interest, ROI), while the high voxel resolution (0.6 μm) scanning is for obtaining the detailed morphology of the crack tip and crack opening displacement (COD).

The cracks were segmented out in Avizo commercial software, using the combination of seeded region growing techniques and global thresholding using the ISO 50% techniques [22]. A direction ray casting technique was used to acquire the COD by projecting the number of voxels representing the crack along a line perpendicular to the crack face [23, 24].

Table 4 parameters of the Xray CT scans

Parameters	Overview scanning	High-resolution scanning
Energy	160 keV	160 keV
Voxel resolution	2.035 μm	0.66 μm
Scan time	4 h	62 h
Field of view	~2.04 × 2.04×2.04 mm^3	~0.66 × 0.66×0.66 mm^3
Number of projections	1601	2401
Exposure time	7 s	90 s
Detector binning	1 × 2	1 × 2

3 Results

3.1 High-temperature long fatigue crack growth and fracture surface observation

The microstructure of the directionally solidified CM247 LC superalloy is shown in Fig.2 where polished and etched samples were observed using optical and scanning electron microscopy. The primary dendrites are aligned parallel to the <001> solidification direction in Fig. 2 (a) with the same primary growth orientation and their cross-section on the surface perpendicular to the solidification direction can be seen in Fig. 2 (b) showing the secondary dendrite arms and varying secondary orientations of the columnar grains. Carbides are found

located at the grain boundaries and the inter-dendritic regions as shown in Figs. 2 (c), (d) and (e). The cubic γ′ strengthening precipitates are clearly observed in Fig. 2 (d). The chemical composition analysis of these precipitates are reported in detail in our previous work [22].

The high-temperature long fatigue crack growth rates versus the stress intensity factor range (ΔK) are plotted in Figs. 3 (a). For the 10 Hz (high frequency) fatigue tests, the crack starts growing at the initial ΔK of 15 MPa√m for both L and T samples at 650 °C and 725 °C. However, fatigue cracks arrest at the same ΔK value, when the test frequencies are decreased to 0.25 Hz (1-1-1-1 waveform) and 0.011 Hz (1-90-1-1 waveform). One typical curve for an L sample tested under a 1-1-1-1 waveform at 650 °C is presented in Fig. 3 (a). After the crack arrests at a ΔK of 15 MPa√m, several steps of increasing the load range by 10% are performed to force the crack growth. Nevertheless, the crack is still unable to propagate until the ΔK reaches nearly 23 MPa√m. The vertical line highlighted by a red dotted ellipse in Fig 3 (a) shows one example of the crack arresting process. Initially increasing the load to give a ΔK of 21 MPa√m, the fatigue crack starts to grow, but crack growth rate dramatically decreases from 10^{-5} mm/cycle to 10^{-8} mm/cycle with only a few more cycles. According to ASTM E 647, when the crack growth rate approaches 10^{-7} mm/cycle, the corresponding ΔK is taken as the threshold

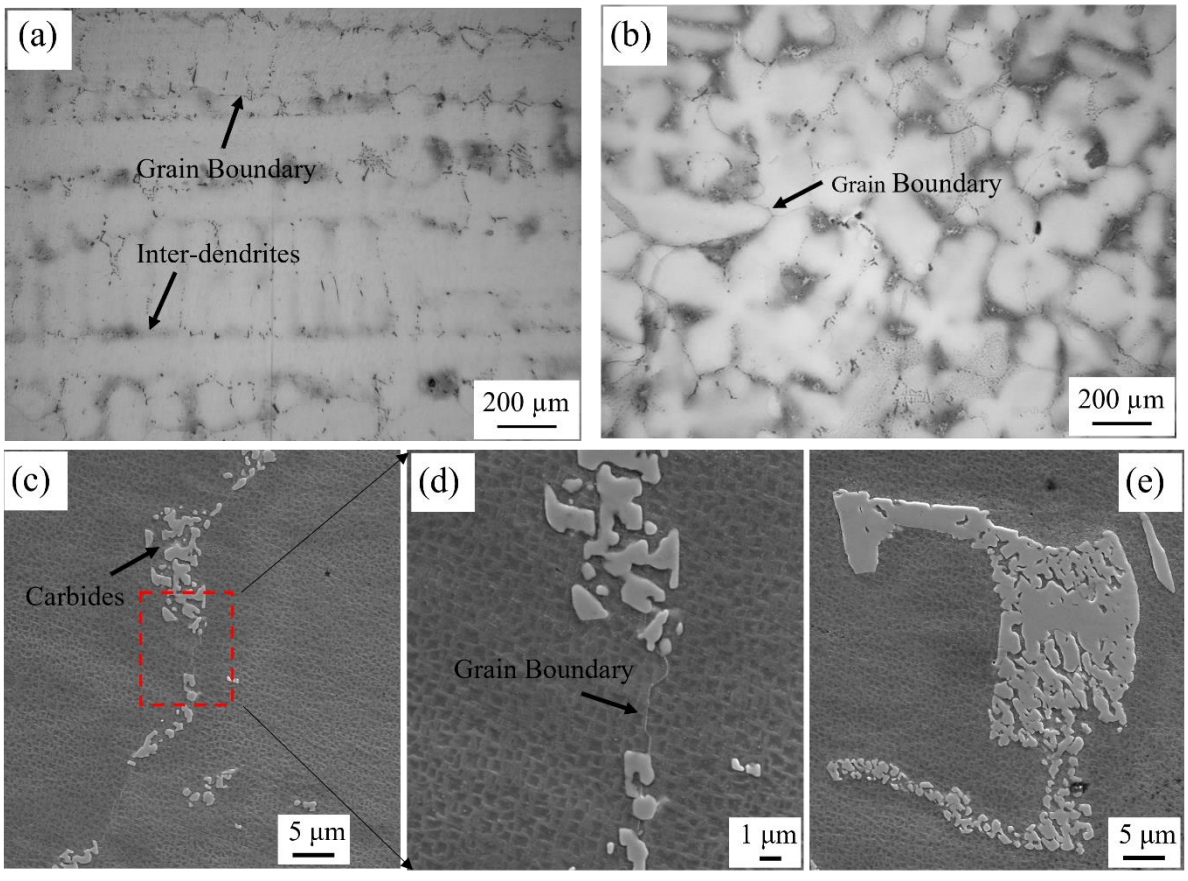

Fig. 2 Polished and etched studies show morphology of dendrites (a) at the surface parallel to solidification direction (b) perpendicular to the solidification direction using optical microscopy and SEM examination showing (c) carbides at the grain boundary (d) morphology of the grain boundary (e) carbides in the inter-dendritic region.

for fatigue crack growth (ΔK_{th}). Apparently, in this case the ΔK_{th} is increasing with the decrease of test frequency. Given that ΔK_{th} is not systematically measured in current work, ΔK_0, denoting the initial ΔK enabling the fatigue crack to grow continuously, is used to describe the severity of crack growth arrests. Figs. 3 (b) shows the relationship between ΔK_0 and test frequencies, in which ΔK_0 increases notably with the decrease of test frequencies for both L and T samples tested at 650 °C and 725 °C. Also, it should be noted that the temperature has an effect on the crack growth arrests. When tested at very low frequencies (1-90-1-1), the ΔK_0 rises from 30 MPa√m at 650 °C to more than 40 MPa√m at 725 °C. Therefore, the fatigue crack growth arrest points are closely associated with both test frequencies and temperatures. Certainly, the microstructure difference between L and T samples has some effect on the

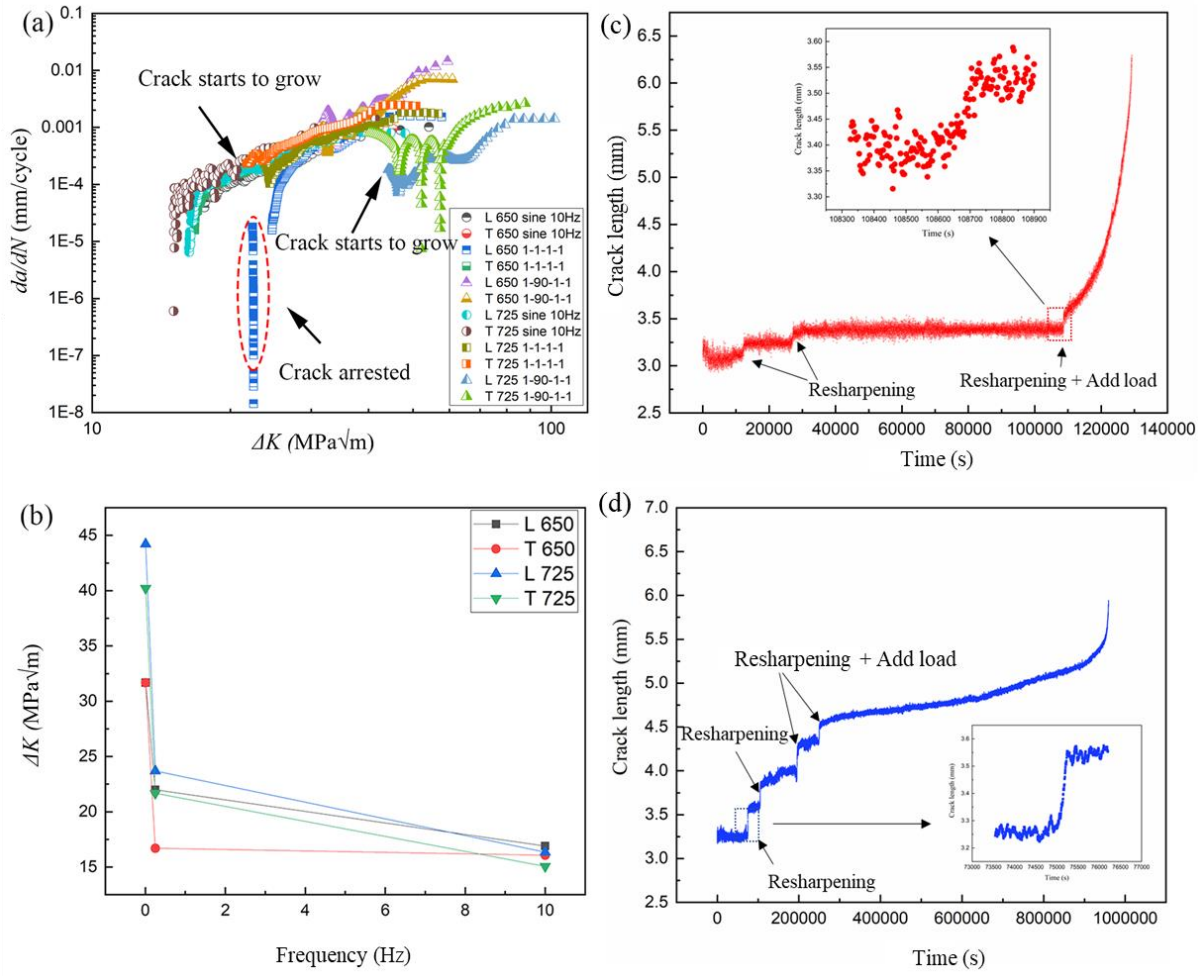

Figs. 3 (a) Fatigue crack propagation rates of L and T samples tested at various conditions, (b) ΔK_0 variation against test frequencies, (c) crack length variation of L tested at 1-1-1-1 waveform, 725 °C and one typical crack tip resharpening process, (d) crack length variation of L tested at 1-90-1-1 waveform, 725 °C and one typical crack tip resharpening process.

fatigue crack growth behaviours. For instance, the T sample doesn't show crack growth arrests at 1-1-1-1 test frequency, 650 °C and L and T samples show much lower fatigue crack growth rates at the 1-90-1-1 test frequency, 725 °C. Compared with the significant effects on crack growth arrests, linked principally to test frequencies and temperatures, the effects of

microstructure alignment are therefore seen to be relatively minor, and are not the focus of current study.

The variation of the crack length records the process of the crack arrests and growth as well as how the ΔK_0 is approached as shown in Figs. 3 (c) and (d) for L samples tested at 1-1-1-1 and 1-90-1-1 waveforms at 725 °C. Arrows in the figures show the points where crack-tip resharpening is performed to force the crack growth. For the L sample tested under the 1-1-1-1 waveform, the first two resharpenings are conducted nearly every 8000 cycles without any detectable crack growth indicated by the stable crack length in Figs. 3 (c). The crack length jumps at the points of crack-tip resharpening, which means the crack-tip resharpening successfully forces the crack to grow. However, after the first two crack-tip resharpenings, the crack is still unable to continuously grow. The crack length is stabilized at 3.4 mm for 25000 cycles, indicating the crack is again arrested. In the third time, to force the crack growth, a simple crack-tip resharpening by changing frequency cannot activate crack propagation and thus, the load range is increased by 10%. The combined methods eventually get the crack to grow and thereafter, the fatigue crack did continuously grow. The ΔK_0 now has been achieved at 23 MPa√m. Another test for an L sample tested under the 1-90-1-1 waveform, shows a similar crack length variation in Figs. 3 (d). In the early stages, the crack could be forced to grow by the crack-tip resharpening by increasing frequency. The combined methods have to be conducted when the test has been sustained for a longer time at this waveform. Finally, the ΔK_0 is increased to nearly 40 MPa√m, which is an extremely high value. Both tests show that the crack-tip resharpening works when the tests have been only conducted for a short time. After a longer duration test, crack-tip resharpening (by frequency increase) should be combined with increasing the load range to obtain the crack growth. Thus, the fatigue crack arrest level is also related to the time of being tested (so very likely linked to crack wake or crack tip oxidation events which develop over time). Two typical crack length extensions caused by the resharpening are displayed as inset graphs in Figs. 3 (c) and (d).

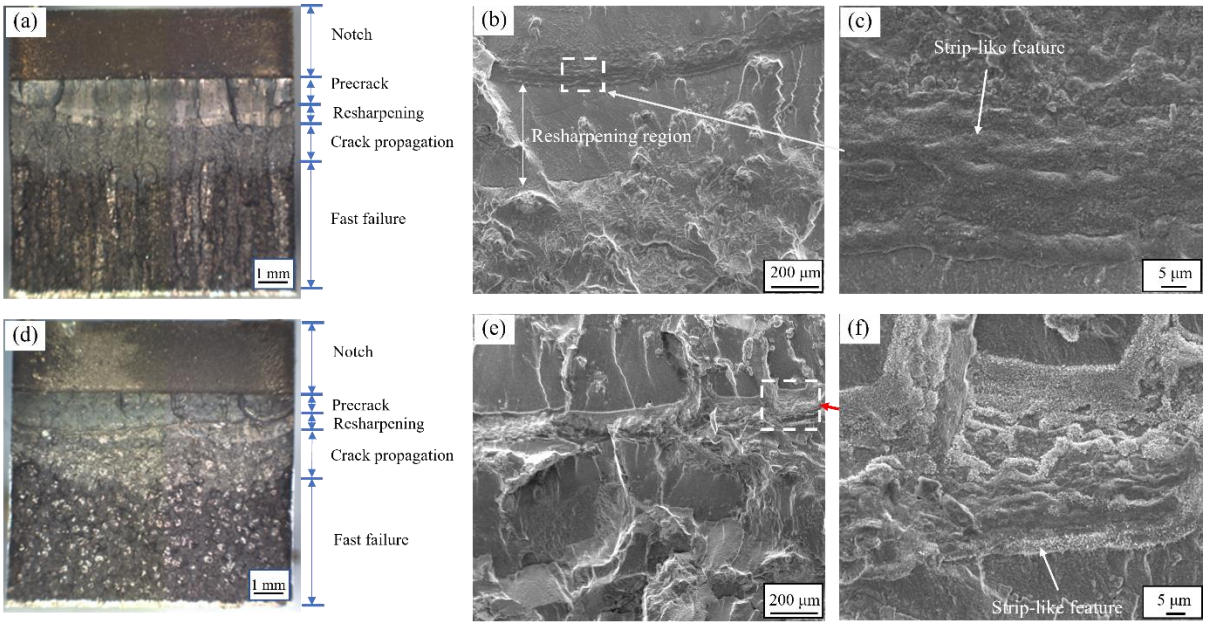

Figs. 4 Optical microscopic (OM) image of T and L samples tested at 1-90-1-1 waveform, 650 ℃ (a, d), the low-magnification SEM images of the resharpening region for T and L samples (b, e), the high-magnification SEM images of oxidation layers for T and L samples (e, f)

Two typical fracture surfaces are shown in Fig. 4. They are L and T samples tested with the 1-90-1-1 waveform, 650 ℃. For both tests, cracks are arrested when the loading frequency is transfered from 10 Hz sine waveform for precrack to 1-90-1-1 trapezoidal waveform. Load range was increased in 10% increments multiple times to force the crack growth to continue, although no detectable crack growth was found. Eventually, the crack did continuously grow, after ΔK_0 is increased to nearly 30 MPa√m, combined with crack-tip resharpening. The features of these crack arrests are clearly observed on the fracture surfaces shown in Figs. 4 (a) and (d). Strip-like features are noticeable at the crack-arrested regions for both L and T samples shown in Figs. 4 (b), (c), (e) and (f). These features are inferred to be oxidation layers formed during the low-frequency tests with a width of over 10 μm. It is inferred that the crack arrest behaviour is associated with the formation of the thick oxidation layers. Thus, more interrupted tests were performed to analyse the oxidation behaviours at the crack tips in more detail.

3.2 Interrupted tests and crack tip characterization

Three interrupted tests were performed. The first one is an L specimen tested under a 1-1-1-1 waveform, 650 ℃ for 48 hours, without detectable crack growth. The total cycles experienced by the interrupted L sample is twice the life time of the L sample tested under a 10 Hz sine waveform. The tested and polished sample is shown in Figs. 5 (a). The interdendrites are generally perpendicular to the main crack propagation direction (indicated by the top arrow in the figure). The main crack is locally tortuous, due to the crack paths following the slip systems or deflected by microstructure features (like carbides or pores). A higher magnification of the crack tip and element maps are shown in Figs. 5 (b). The morphology of the crack tip is noticeably different to the expected sharp crack tip. It shows a round-coronal morphology with oxygen filling the whole crack, indicated by the oxygen-distribution map. Obviously, the crack tip is blunted. The Ni and Co-element distribution maps demonstrate that the Ni/Co-rich oxides are mainly located within the crack tip, forming the so-called external oxidation layers. The Al/Cr-rich oxides are formed ahead of the crack tip at the coronal parts, which is potentially caused by the intrusion of oxygen species into the alloy ahead of the crack tip.

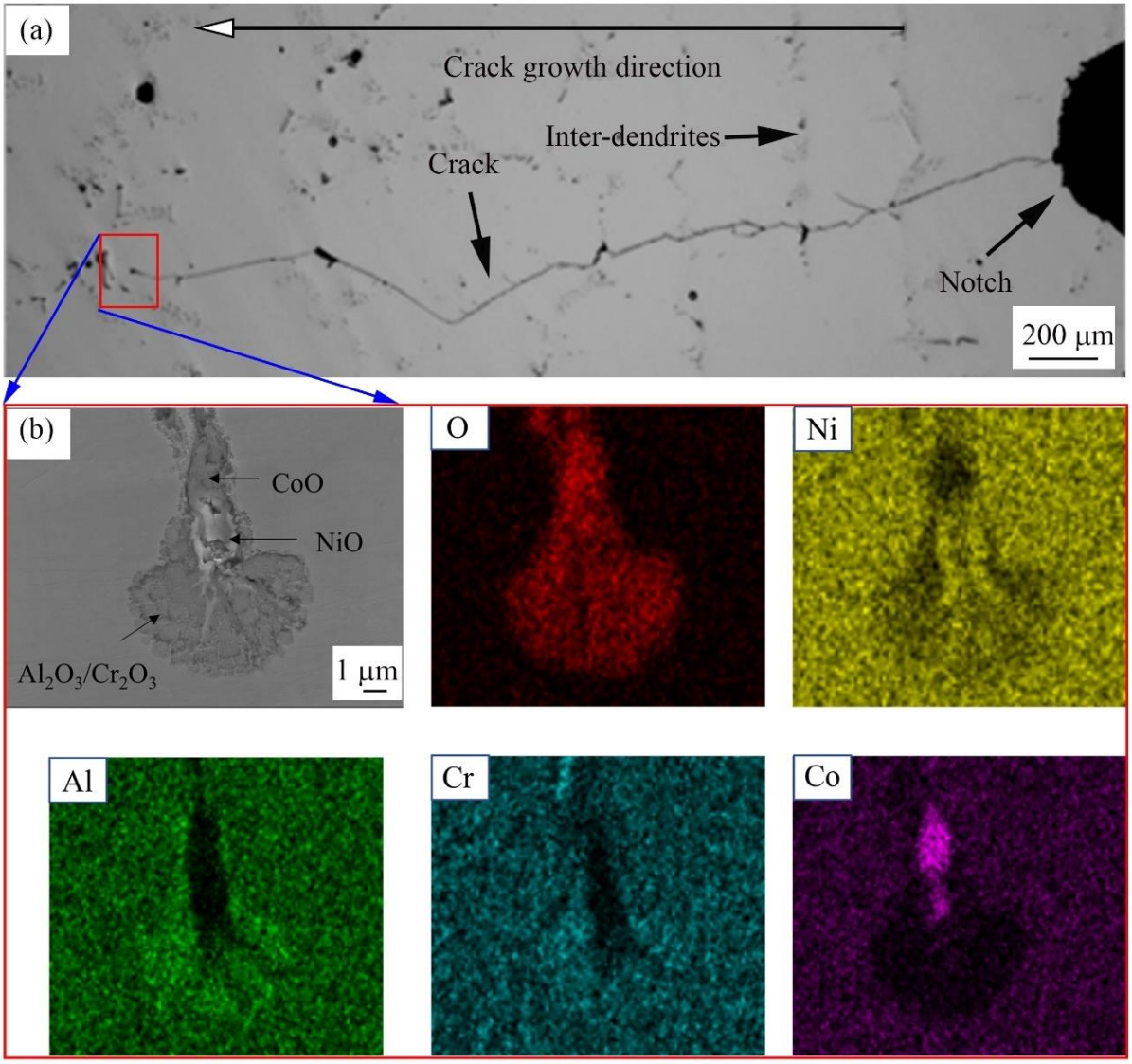

Figs. 5 (a) the OM image of interrupted L sample after tested at 1-1-1-1 waveform, 650 ℃ for 48 hours, (b) the high magnification SEM image of the crack tip and associated element distribution maps.

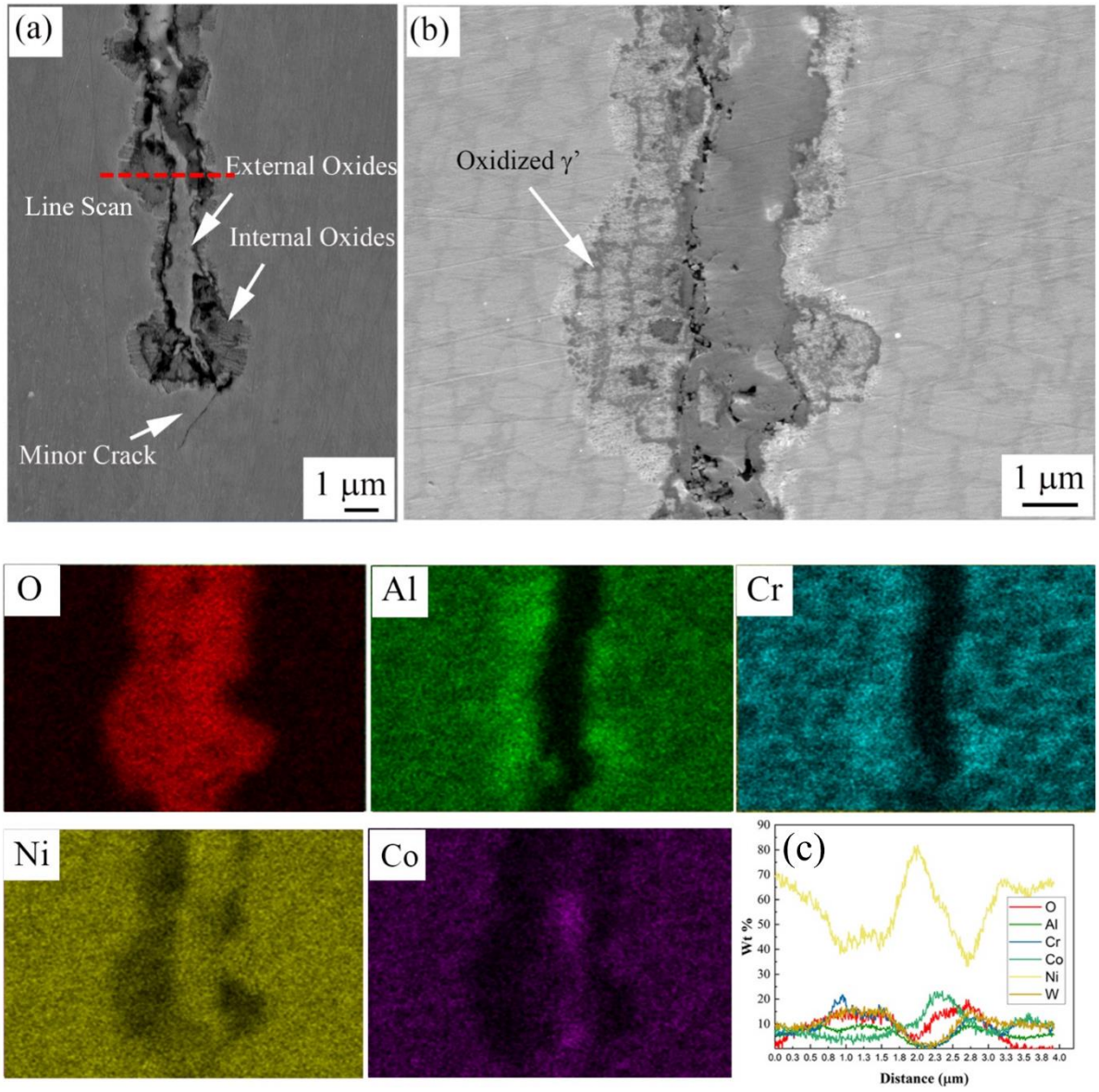

Figs. 6 SEM images of the crack tip of interrupted T sample, tested at 1-90-1-1, 650 ℃ for 12 hours (a), and the crack wake and associated element distribution maps (b), an EDX line scan perpendicularly across the crack (c).

For the second interrupted test, the T sample is interrupted after being tested under a 1-90-1-1 trapezoidal waveform, 650 ℃ for 12 hours, similarly without any detectable crack growth. The crack tip has a round-coronal morphology as well (Fig. 6 (a)), with however, a smaller size compared to the crack tip of the first interrupted-test sample. The diameter of the round-coronal region of the crack of the L specimen is approximately 6 μm, determined by measuring the longest distance between two points within the coronal region. Comparatively, the diameter of the crack tip in the second interrupted sample is only ~ 3 μm. In addition, a very minor crack is found in front of the coronal crack tip in Figs. 6 (a), indicating potentially the crack growth is not completely arrested, but it should be noted whether the minor crack is formed before the oxidation of the crack is uncertain due to the 2D section being assessed here. A higher-magnification SEM image of the crack wake, taken under a lower accelerated voltage, more clearly presents the morphology of internal and external oxides in Figs. 6 (b). The completely oxidized γ′ precipitates and γ channel constitute the internal oxidation layers.

Associated element distribution maps show the enrichment of Al and Cr elements in the same region. The composition of the external oxidation layers is as observed in the L samples, consisting of Ni/Co-rich oxides. An EDX line scan is performed at the crack wake, perpendicular to the crack propagation direction, marked in Figs. 6 (a). According to the element variation along the line profile in Figs. 6 (c), the thickness is measured to be 1.2 μm for external oxides and 2.0 μm for internal oxides. Herein, the EDX line scan is employed as a tool to measure the thickness of oxides and performed multiple times to obtain statistically consistent data.

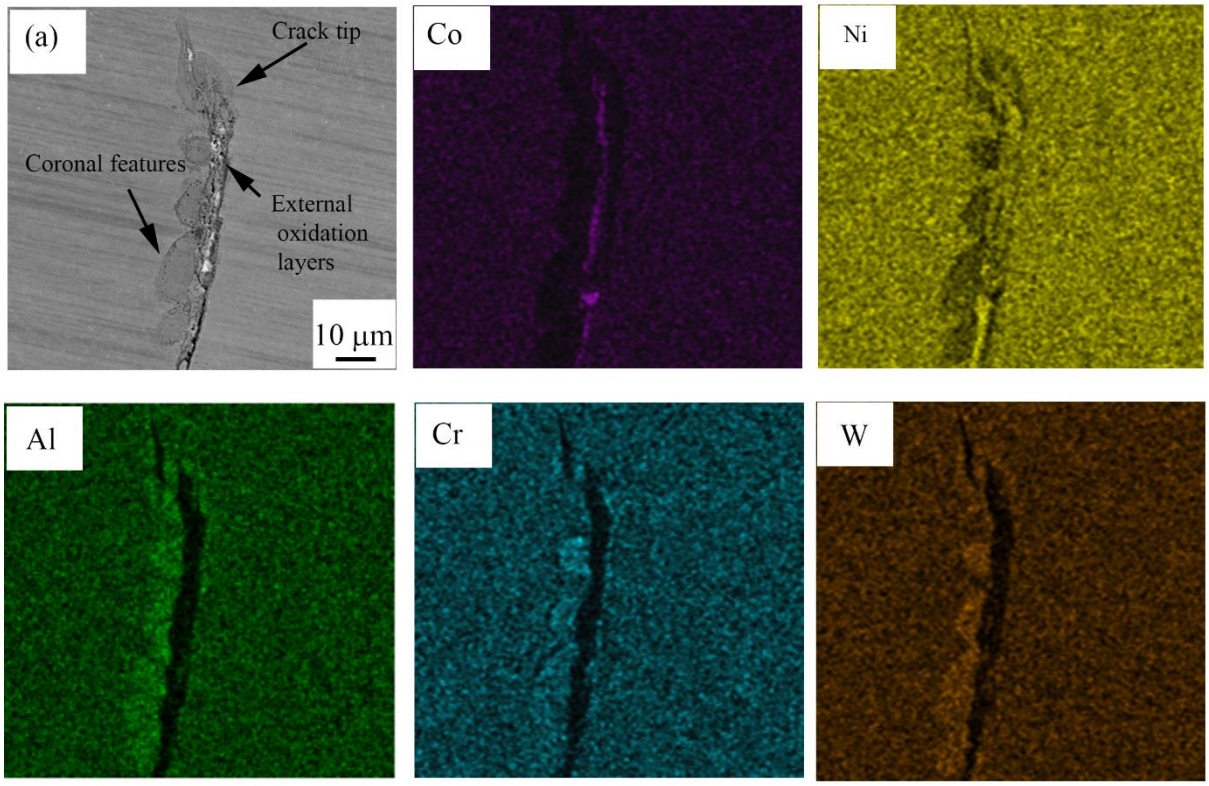

Figs. 7 the SEM image of the crack tip for the third interrupted T sample, tested at 1-90-1-1, 650 ℃ for 96 hours and associated element distribution maps.

The third interrupted test is much more complicated. The T sample was tested at 1-90-1-1 waveform, 650 ℃ for, in total, 96 hours. Load range was increased by 10%, during the test approximately every 16 hours, and eventually the ΔK reached 24 MPa$\sqrt{m}$. A series of round-coronal oxidized features are observed in a row along the crack tip shown in Figs. 7 (a). However, these features are formed at both crack tip and wake, apparently different to previous tests, where internal oxidised regions are only formed at the crack tip. It indicates that the crack did indeed grow after load was added, but the growth length is in micron scale, undetectable by the potential drop method. After a few microns growth, the crack is arrested again, forming the round coronal crack tip. The number of the coronal features is consistent with the number of times the load range was increased. The element distribution maps present similar oxidation layers as the last two cracks, but the thickness of the external oxidation layers is increased to approximately 4 μm. This could be attributed to the larger crack opening caused by the higher ΔK value.

3.3 Three-dimensional characterization of the crack tip via X-ray computed tomography (X-ray CT)

The SEM-based characterization illustrates the formation of thick oxidation layers at the crack wake as well as at the crack tip. However, this two-dimensional characterization is sectioning-position dependent, and reconstructing the crack tip in three-dimensions could obtain more valuable/relevant information, especially measuring the crack opening displacement (COD) systematically. The 3D rendering of the crack tip of the interrupted L specimen tested under 1-1-1-1 waveform, 650 ℃ is shown in Figs. 8 (a). The crack propagation and loading direction is marked in the figure, and it is notable that the crack tip is not as sharp as those observed in polycrystalline superalloys using X-ray CT, tested under similar conditions [25]. Slices corresponding to the different positions of the crack tip are presented in Figs. 8 (b), (c), (d) and (e). All the CT slices show the rounded crack tips, consistent with the observation via SEM.

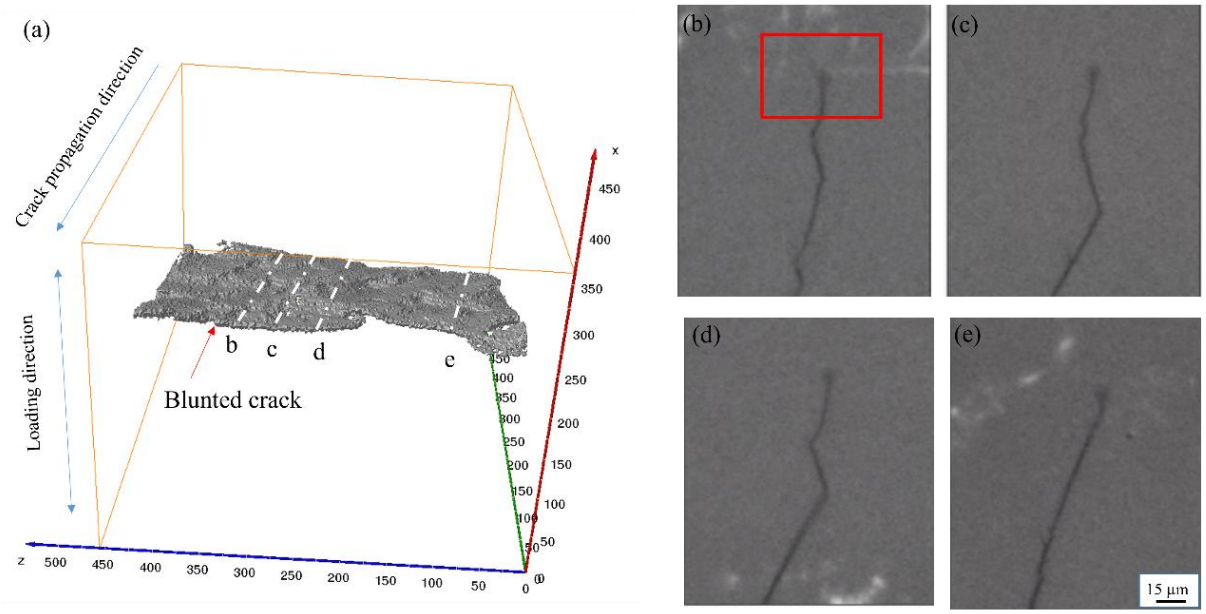

Figs. 8 (a) CT 3D rendering of crack profile for the interrupted L sample, tested at 1-1-1-1 650 ℃ for 48 hours, slices corresponding to the line profiles: b (b), c (c), d (d), e (e).

Another 3D rendering of the crack tip of the interrupted T sample tested at 1-90-1-1 waveform, 650 ℃ after 96 hours is shown in Fig. 9 (a). It is interesting that the tiny match-stick sample possesses two cracks, which is potentially associated with the large columnar grain structure. The columnar grains aligned with the crack propagation direction facilitate crack initiation and propagation inside each grain[22]. Similarly, the blunted crack tips are observed in both the 3D rendering and the corresponding slices. In comparison, the scales of the blunted crack tips are considerably larger than those in the L sample due to the longer time exposure to the high temperature. Also, the blunted crack tips are elongated, attributed to increasing the load range several times during the test (to try and grow the crack). The slice d (Figs. 9 (d)) shows the two-crack overlaid region, where both the crack tips are rounded.

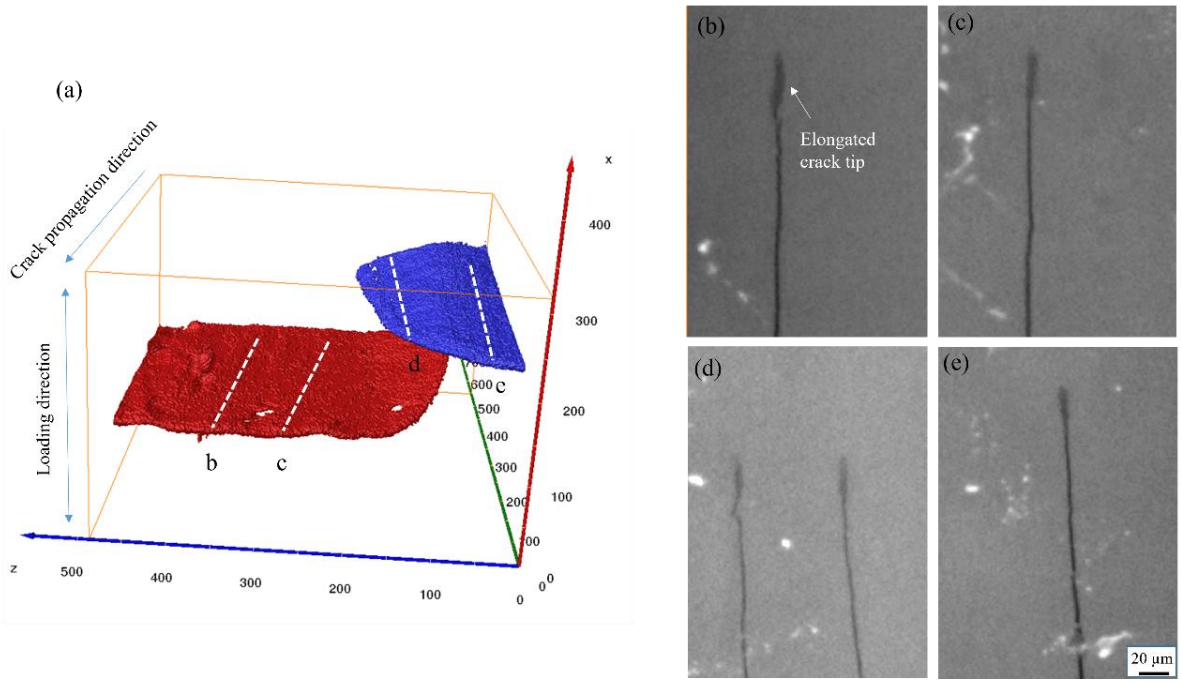

Figs. 9 CT 3D rendering of crack profile for the interrupted T sample, tested at 1-90-1-1 650 ℃ for 96 hours, slices corresponding to the line profiles: b (b), c (c), d (d), e (e).

The COD contour maps measured perpendicular to the crack plane (Figs. 10 (a) and (b)) show the high values at the crack front lines for both L and T samples. In comparison, the front line of high CODs is wider in the T specimen, consistent with the elongated crack tip observed by SEM and X-ray CT. Corresponding line profiles across the crack faces are shown in Figs. 10 (c) and (d). The peak COD values are presented at the interface between the crack faces and the materials matrix, confirming the formation of the round crack tips for both L and T samples. It is notable that the peak COD values of the crack tip are over 12 µm for T sample, while around 7 µm for L sample. This is potentially caused by the longer duration and higher K_{max} of the test leading to the larger oxidised region at the wake of the crack tip. The line profiles of the L sample are noisier, and at some points, the COD reaches zero, indicating the direct contact between crack faces without oxidation formation. The CODs of the crack wake vary with the distance to the crack tip. The values rise from 0 - 2 µm, within the distance of 50 µm to the crack front line (herein, the crack front line is considered at the COD peak point) to 4 - 6 µm, with the distance increasing to 200 to 300 µm. T sample exhibits the similar trend for the CODs, as they are nearly 4 - 6 µm within the distance of nearly 100 µm, while increase to 6 - 8 µm at a larger distance. Therefore, the difference of CODs is mainly concentrated at the crack wake within a short distance (less than 50 µm) to the crack tips for L and T samples.

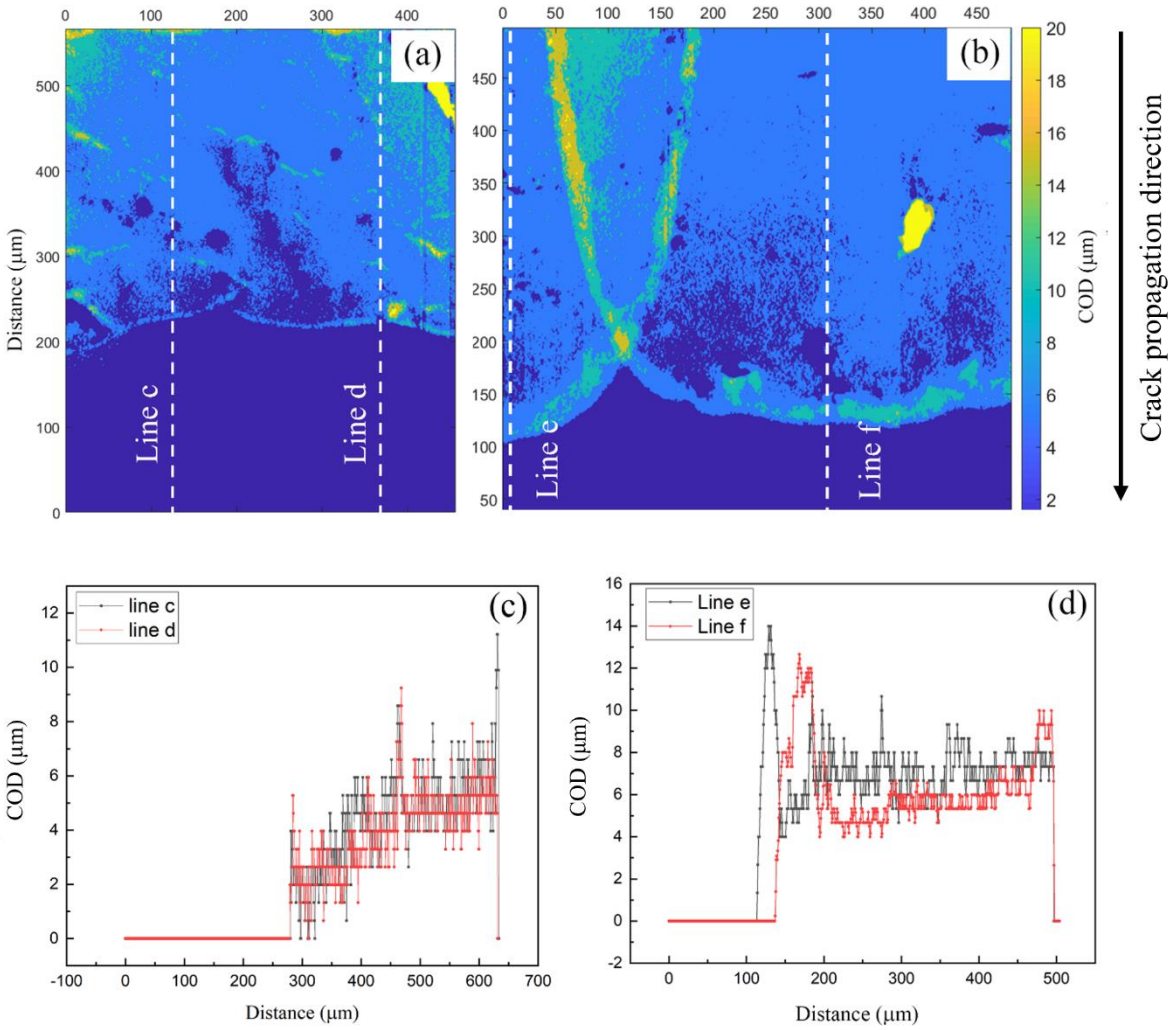

Figs. 10 Crack opening displacement plots across the crack face for interrupted L sample, tested at 1-1-1-1 650 ℃ for 48 hours (a) and T sample, tested at 1-90-1-1, 650 ℃ for 96 hours (b), COD line profile plots as measured across the white dotted lines for L (c) and T (d).

4 Discussion

The above work provides clear experimental results confirming the existence of significant oxidation-induced crack closure (OICC) under high temperature and low frequency testing conditions in a Ni base superalloy. Over the past few decades, oxidation has tended to be regarded as a purely detrimental process prompting fatigue crack initiation and propagation at high temperatures [3-7, 26]. Although some research shows evidence of oxidation-induced crack closure results [16-20, 27], particularly in the 1980s, the underlying mechanism was somewhat ambiguous due to the lack of characterization techniques of high enough spatial resolution and inability to consider the full 3 dimensional process. A question also arises as to whether the deceleration of the crack propagation is caused by the oxides filling the crack wake or the effective increase of fracture surface roughness by the oxidation (roughness-induced crack closure). Current work rationalises the crack closure results based on the OICC mechanism combined with the benefits of detailed characterization. Modified models and

solutions are proposed and discussed to understand the physical mechanisms and chemical reactions behind the OICC.

4.1 Complete or partial oxidation-induced crack closure?

In considering general fatigue crack propagation without oxidation, the crack opening displacement (COD, δ) reaches a peak under the maximum load, denoted as δ_{max}, while the lowest value is seen at the minimum load, δ_{min}. The difference between the CODs ($\Delta\delta$) at the maximum and minimum loads could act as the parameter indicating the driving force for the crack advancing [28]. However, once the oxidation film is formed at the crack flanks, the δ_{min} is accordingly increased, decreasing the $\Delta\delta$ and driving force for the crack propagation. The whole process is shown in the schematic diagram Fig. 11. Although the mechanism was proposed a few decades ago [16-18, 27], quantitatively evaluating the effects of OICC on fatigue crack propagation is still a challenge. According to N. Louat et. al [21, 29, 30], there are at least two cases that need to be considered when evaluating the OICC. They are termed as complete oxidation-induced crack closure (COICC) and partial oxidation-induced crack closure (POICC, this was termed as asperity induced crack closure in some literature [21, 29]), respectively. Whether the formed oxides inside the crack wake are continuous or discrete is the critical difference between COICC and POICC. Researchers think COICC is an idealised model [29], as usually the oxides inside the crack are believed to be formed by 'fretting oxidation', which means the oxide scale is repeatedly breaking and reforming under the cyclic loading. In this case, a continuous oxide film is rarely formed, and hence very few models have been proposed to assess the effects of COICC. Nevertheless, the current study clearly shows the continuous external oxidation layers formed within the crack for our 1-90-1-1 tests in Figs. 6 (a), (b) and Figs. 7 (a). It should be noted that these SEM images are at high magnifications, only showing local oxides within the crack. In addition, the 2D observation is sectioning-position dependent, thus requiring a more systematic characterization evidencing the occurrence of COICC. The COD measured using X-ray CT could provide such systematic data, proposed by Toda et. al [23, 24]. For the tests of 1-90-1-1 loading frequencies, the randomly selected line profiles of the crack faces indeed show stable and high COD values, as shown in Figs. 9 (d), indicating the formation of continuous oxides wedging the crack opening. In contrast, for the tests under the 1-1-1-1 loading frequencies, the COD values fluctuate significantly, and at some points of the line profiles, the COD values reach zero in Figs. 10 (c), indicating the contact of the crack faces. The stitched image of the crack path of the 1-1-1-1 test also confirms this in Figs. 12 (a). Therefore, the occurrence of COICC or POICC is highly dependent on the test frequencies for the alloy. The relatively high-frequency tests are more likely to smash the oxides repeatedly, resulting in POICC, while low-frequency tests will facilitate the formation of thick and continuous oxides, leading to COICC. Based on the results, different models and solutions are proposed to evaluate the effects of COICC and POICC.

4.2 The effects of the COICC

Firstly, for the COICC, where the COD is rather stable, the following simplified assumptions are made:

(i) The δ_{max} is only related to the maximum load, not affected by the oxidation.

(ii) The δ_{min} is equal to the thickness of the external oxidation layers, as the oxides are assumed to be rigid bodies.

(iii) The thickness of the external oxides is taken as the average oxide thickness within 10 μm behind the crack tip.

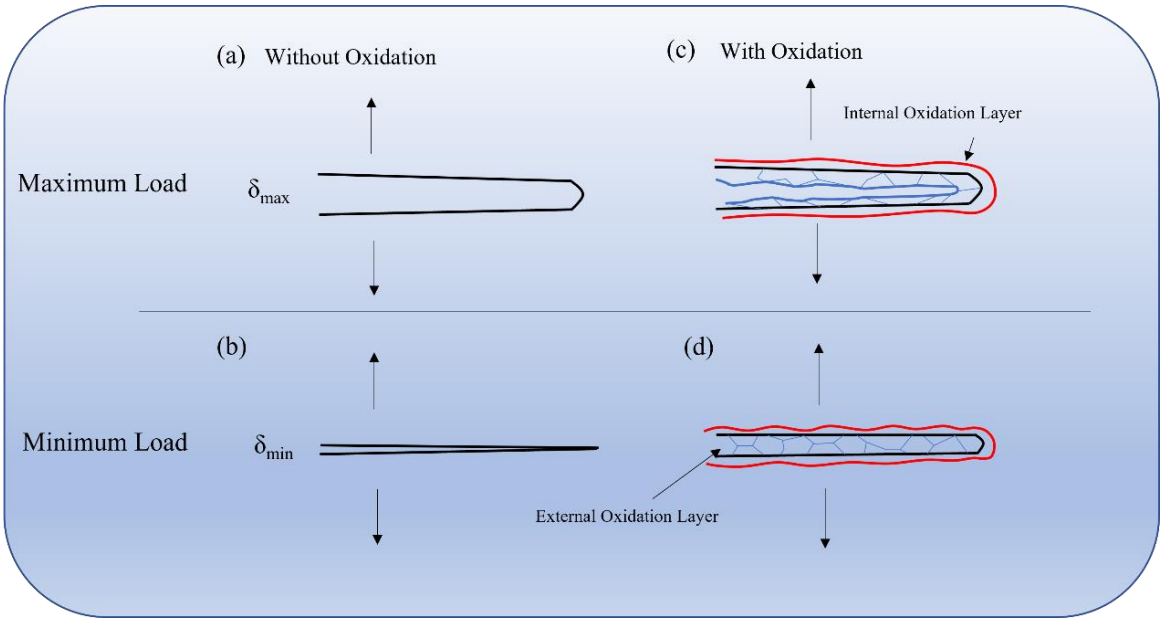

Figs. 11 Schematic diagram of fatigue crack opening at maximum load (a) and minimum load (b) without oxidation, maximum load (c) and minimum load (d) with oxidation.

From the SEM characterization results, internal oxides are formed by the oxygen intrusion into materials, slightly affecting the crack opening. Thus, the effects of internal oxides are not considered here, but will be discussed later. Approximating the δ_{min} with the oxide's thickness is supported by Suresh et. al [16], but theoretically, calculating the δ_{min} should consider the external oxide's thickness as well as the CODs induced by the minimum load. Given that the load ratio, R is only 0.1, the δ_{min} induced by minimum load is negligible compared with the δ_{max} and the oxide's thickness in the second assumption. The third assumption is associated with the definition of COD, as the values always increase from the crack tip to the crack end. Most researchers think that the driving force for the fatigue crack propagation is mainly influenced by the COD near the crack tip, termed as CTOD. In most cases, the CTOD is defined at the points where a 90° angle at the crack tip intersects with the crack sides [31]. However, due to the oxygen intrusion, the crack tip is blunted and forms a distinctive rounded shape, completely different to the normal sharp crack tip (Figs. 5, 6, 7, 8, 9). Thereby, using the method of 90°-intersected lines might overestimate the CTOD. According to the CODs measured from X-ray CT in Figs. 10 (c) and (d), the δ_{min} is stable within distance of 50 μm to the crack tip. Herein, the δ_{min} (external oxides thickness) is measured in two ways. The first way is measuring the δ_{min} by averaging the thickness of external oxides within 10 μm to the crack tip via SEM-EDX. The other is directly measuring the average δ_{min} of the equal region

using X-ray CT. It should be noted that there is an obvious oxidation intrusion ahead of the crack tip, which is incapable of being distinguished by X-ray CT. To avoid counting the oxidation intrusion into crack, all the COD measured by X-ray CT is extracted 10 μm behind the segmented crack tip. The averaged oxidation intrusion size is in the range of 6 μm to 9 μm. The stress intensity factor K_c, when crack flanks contact oxides, and effective stress intensity range (ΔK_{eff}) are calculated based on the measured oxide's thickness, using the following equations:

$$K_{max} = \frac{P_{max}}{B \times W^{1/2}} \times Y \times 10^{1.5} \quad (1)$$

$$\delta_{oxides} = \frac{K_c^2}{m\sigma_Y E'} \quad (2)$$

$$m = 1.517\left(\frac{\sigma_Y}{\sigma_U}\right)^{-0.3188} \quad (3)$$

$$\Delta K_{eff} = K_{max} - K_c \quad (4)$$

where K_{max} is the stress intensity factor at the maximum load, P_{max} is the applied maximum stress, B is the breadth of the cross-section of the bend bar, W is the height of the cross-section of the bend bar, Y is the stress intensity factor function given by British Standards [32], m is the parameter associated with the material's yield stress, σ_Y and ultimate failure stress, σ_U. E' is the Young's modulus under plane strain conditions [33]. δ_{oxides} is the thickness of oxides measured using SEM-EDX. They have been compared with COD data extracted from X-ray CT in Figs. 12 (d). It is obvious that the data from X-ray CT overestimates the COD values, potentially caused by two factors. The first one is the partial volume effect existing in segmenting the crack [23], causing an error of half the voxel size at maximum (0.3 μm in the current work). The second one is the oxygen intrusion along the crack, leading to the formation of internal oxidation layers with width of nearly 2 μm in Figs. 6 (a), (b) and Figs. 7 (a). Completely segmenting the crack from the internal oxidation layers is unachievable due to their extremely close grey values, and hence resulting in the overestimation of COD.

Table 5 δ_{oxides} from SEM and $\Delta\delta$ calculated from the ΔK applied for the fatigue tests, ΔK_{eff} and ΔK

	*Thickness of oxides	Δδ calculated from ΔK	ΔK_{eff}	ΔK
T interrupted after 12 h	1.09	1.53	3.88	15.07
T interrupted after 96 h	2.61	3.30	4.75	22.18

* The unit for thickness of oxides and COD are μm, for ΔK_{eff} and ΔK is MPa√m

The measured average thickness of external oxides is quite close to the $\Delta\delta$ calculated from ΔK in Table 5, indicating the significant effects of crack closure induced by external oxides. Calculated ΔK_{eff} values directly confirm the hypothesis, as the markedly reduced ΔK_{eff} is apparently lower than the common ΔK_{th} quoted for superalloys [34-36], illustrating the arrest of the crack growth at low frequency. The good fit of experimental results and calculations validates the use of this simplified geometrical model, which could be employed in other similar material systems for evaluating COICC.

4.3 The effects of the POICC

As discussed above, POICC occurred during the test at 1-1-1-1 frequency. Figs. 12 show the locations of these asperities. It is worth noting that oxidation intrusion along the crack wake is much slighter compared with the test of 1-90-1-1, and thus COD from X-ray CT is comparable with the oxide's thickness measured from SEM-EDX in Figs. 12 (e). Evaluating the POICC is far more complicated than COICC, and so far, only two models have been proposed, which attempt to quantitively correlate the thickness of oxides on the driving force for fatigue propagation. One of them is proposed by Suresh et. al [16, 37], where only a mechanical closure phenomenon arising from the oxide wedge is considered. The K_c at the crack tip is calculated based on elastic superposition using the Westergaard stress function:

$$K_c = \frac{E'd}{4\sqrt{\pi l}} \tag{5}$$

$$\Delta K_{eff} = K_{max} - K_c \tag{6}$$

where d is the height of the rigid wedge, $2l$ is the location behind the crack tip. Herein, the COD data measured using X-ray CT is utilized to calculating the ΔK_{eff} under the effects of oxides in different positions. The scattered ΔK_{eff} shown in Figs. 12 (f) is due to the thickness variation of oxides within the crack, which is the feature of POICC. Some points with fine-scale oxides lead to a high ΔK_{eff} value, while some points with large-size cause a significant crack closure (low ΔK_{eff} value). However, the scatter in ΔK_{eff} tends to converge to 0 with oxides positioned close to the crack, indicating even small oxides forming at the crack tip will exert a significant closure effect on the crack propagation. It is consistent with the experimental results that the fatigue crack is arrested with external oxides forming extremely close to the crack tip in Figs. 12 (d). The ΔK_{eff}, resulting from the oxides located more than 200 μm behind the crack tip, becomes more stable, varying in the band between 8 MPa√m to 12 MPa√m. This is attributed to the more stabilized COD data measured at these positions shown in Figs. 10 (d). Although the COD data far behind the crack tip is higher, their effect on crack closure is much slighter. It is worth noting that Suresh's model is based on linear elastic theory, which is unable to describe the K_c in the plastic region. The radius of cyclic plastic region is estimated to be 9.1 μm [38]. In this case, using the data obtained 10 μm behind the crack tip to calculate ΔK_{eff} is reasonable.

Louat et. al [29, 30, 39] proposed a nonlinear elastic model to calculate POICC, based on the dislocation continuum theory. In Suresh's model, they thought once the crack faces contact with the rigid body during the unloading process, the whole crack is blocked from further closing. In comparison, Louat et. al thought that the contacted parts of the crack are open, while other indirectly contacted parts are going to further close. It results in the dislocation density for indirectly contacted parts being considered to be zero, but for contacting parts should be related to the Burgers vector and heights of the oxide. Based on the hypothesis and some simplified assumptions, the ΔK_{eff} could be calculated using following equations:

$$\Delta K_{eff} = K_{max} - 0.25K_i[1 + 0.75\left(\frac{K_{min}}{K_i}\right)] \quad (7)$$

They thought when the crack faces contact the oxides, there should be a slope change of the cyclic strain-stress at the unloading phase. The stress intensity factor corresponding to the inflection point is K_i. Nevertheless, the inflection point is hard to distinguish in the experiments for the material [40], as the effects of the local crack closure on the global mechanical response of the material should be minor, particularly at the initial stage of crack propagation tests. Herein, another experimental solution to estimate the K_i is proposed in the current paper based on the COD data obtained using X-ray CT. Essentially, the K_i is exactly the point when oxides are contacting with crack faces, hence it could be calculated if the CTOD of that point could be measured. In the model shown in Fig. 12 (g), the initial contact between crack faces and oxides is considered, and thus the CTOD at the position 10 μm behind the crack tip could be calculated using following equation:

$$\delta_{10} = \delta_{COD}\frac{10}{l} \quad (8)$$

where δ_{10} is the CTOD at the position 10 μm behind the crack tip, δ_{COD} is the COD at the position with distance of l μm to the crack tip. Then the K_i could be calculated using equation (2) and (3). The contact between oxides and crack faces could occur at many points within the crack, and consequently a series of K_c is calculated based on the CTOD estimated from oxides at different position along the crack. K_i should be in the range of these K_c, and hence the range of ΔK_{eff} could be calculated by replacing K_i with the series of K_c. The calculated ΔK_{eff} is in the range of 10 MPa√m (near the crack tip) to 15 MPa√m (far away from the crack tip) in Figs. 12 (d), which is much higher than that calculated from Suresh's model. It indicates that although the formation of external oxides indeed reduces the driving force, but their effects are not as significant as proposed by Suresh et al. So far, it is still quite a challenge to directly measure the driving force variation in high-temperature fatigue tests, leading to difficulty in validating and developing these models. However, the data calculated from both models show that oxides forming near to the crack tip exert a significant retardation effect on the crack propagation, which is consistent with the current experimental results. It should be noted that the calculated ΔK_{eff} is highly oxide-position dependent according to the two models and thus, systematic data

of oxide thickness and position is required. Current work proves that X-ray CT could be appropriately employed to characterize the POICC, particularly in materials or test conditions where oxygen intrusion is minor.

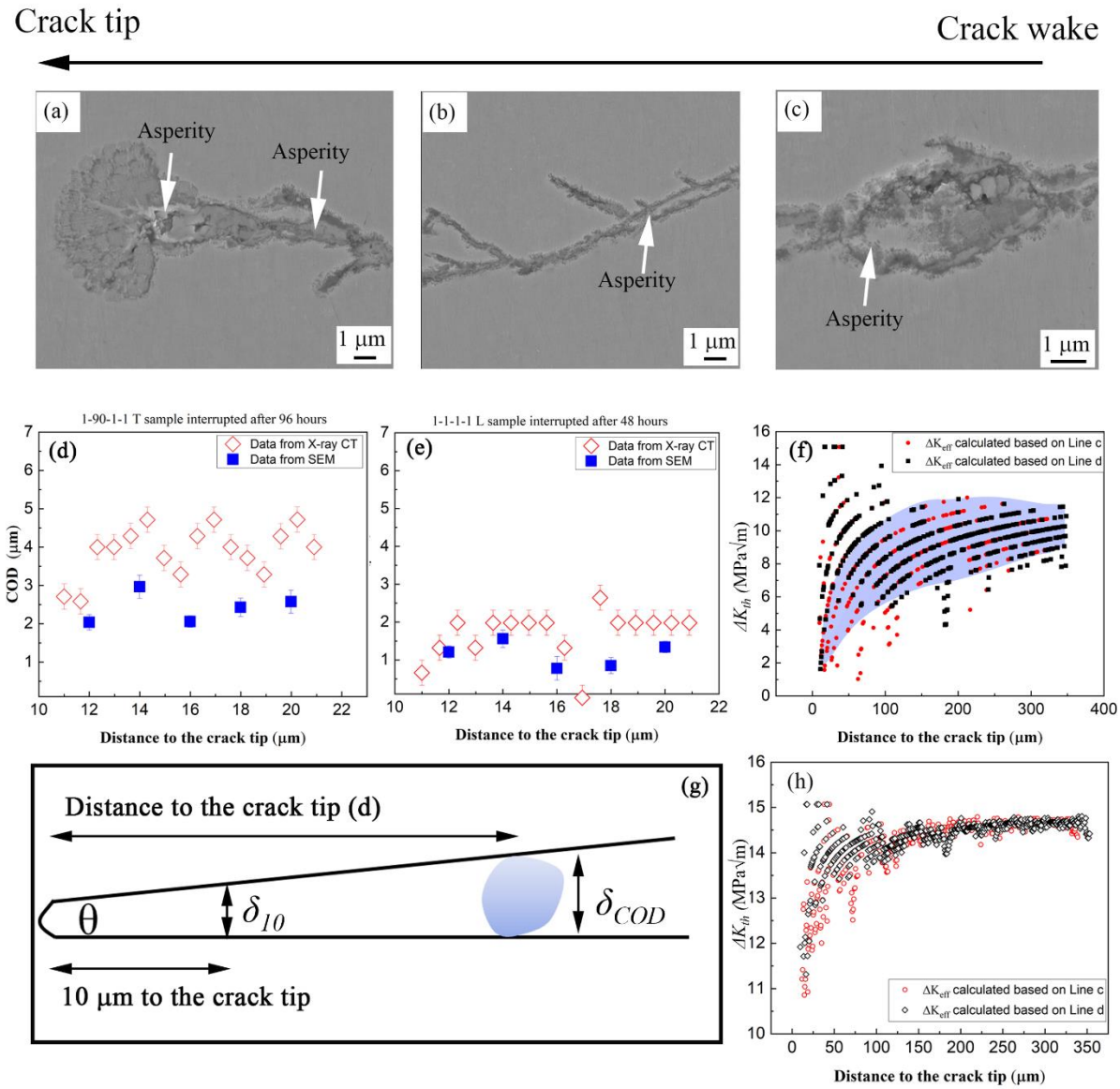

Figs. 12 the SEM images from the crack tip to the crack wake of the interrupted L sample, tested at 1-1-1-1 650 ℃ for 48 hours: (a), (b), (c); COD measured by X-ray CT and SEM-EDX for the L, tested at 1-90-1-1, 650 ℃ for 96 hours (d) and L, tested at 1-1-1-1, 650 ℃ for 96 hours (e); ΔK_{eff} calculated based on Suresh's model (f); Schematic diagram of the model to estimate the CTOD (g); ΔK_{eff} calculated based on Louat's model.

4.4 The effects of microstructure

As discussed above, external oxides play a significant role in arresting the fatigue crack propagation for both L and T samples. However, it should be noted that T sample does not show any crack-arrest phenomenon, tested at 650 ℃ and 1-1-1-1 waveform. This is in contrast to the situation of the L sample, where ΔK needs to be increased to nearly 22 MPa√m to allow crack growth. To confirm this, these tests have been repeatedly performed and show the same results consistently, indicating the crack arrest is also affected by the underlying microstructure.

The precrack path of L and T samples are compared in Figs. 13, derived from 2D X-ray CT tomograph slices. It is obvious that the pre-cracks of the L samples (Figs. 13 (a) and (b)) are much more tortuous than those of the T samples (Figs. 13 (c) and (d)). This should be attributed to the relationship between dendrite orientations and crack propagation direction. For the L direction, the fatigue crack propagates generally perpendicular to the dendrites, and hence, it needs to go across the carbides, located in the inter-dendritic region, e.g. marked by the black arrow in Fig. 13 (a). Obviously, these carbides deflect the crack, resulting in a more tortuous crack path. Comparing with the crack propagation in the L sample, the crack in the T sample can propagate in much straighter trajectory within (and along) the main dendritic regions and largely avoid being deflected by carbides, as shown in Figs.13 (c) and (d). According to [41, 42], these deflection points could act as contact points to induce the crack closure, and hence reduce the effective stress intensity. From this point of view, it is reasonable to deduce that the crack arrest only occurs in L sample at 650 ℃ and 1-1-1-1 waveform, due to the occurrence of both POICC and roughness-induced crack closure acting together.

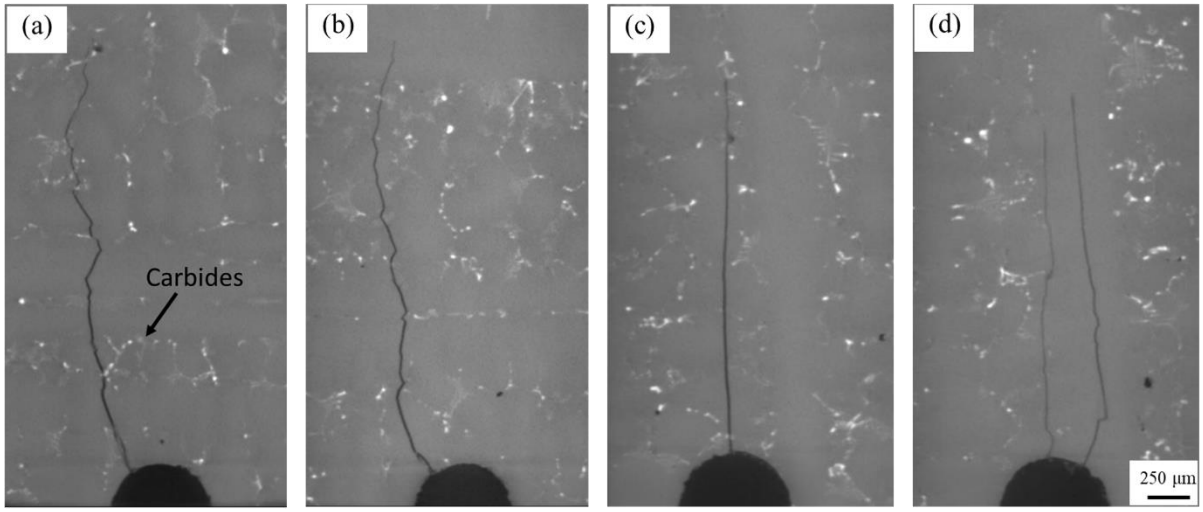

Figs. 13 The precrack path revealed in X-ray CT 2D tomographs of L, tested at 1-1-1-1, 650 ℃ for 48 hours (a) and (b); of T tested at 1-90-1-1, 650 ℃ for 96 hours (c) and (d)

It should be noted the crack paths in Figs. 13 are produced from pre-cracking at high frequency, as both L and T samples were arrested after pre-cracking. The pre-cracking is performed at the same test conditions 650 ^{o}C and 10 Hz waveform. Therefore, this comparable pre-crack test condition can be used to analyse the effects of microstructures on crack paths and consequent crack closure behaviours. Here we have only considered the deflection of the crack path by interdendritic carbides. The crack deflection by propagating into neighbouring grains is not discussed. This is because firstly, the grains of the DS materials are quite large (several hundreds of microns), and the precrack path considered here is ~ 2 mm, therefore in this case grain orientation influence is minor compared to the role of inter-dendritic regions within the large columnar grains. Secondly, the effects of grain orientation are likely to be more complicated, associated with the slip systems and misorientations between neighbouring grains, the current work and cases presented here are therefore mainly focused on the oxidation process.

Future studies are also planned to evaluate the effect of these DS microstructures on a wider set of fatigue crack propagation cases in more detail.

5 Conclusions

The following conclusions can be drawn based on the current work:

(1) Fatigue crack growth is arrested in the low-frequency fatigue tests at 650 ℃ and 725 ℃ in both L and T samples, except for the T sample tested at 650 ℃ and 1-1-1-1 waveform. It has been determined that the external oxides consist of Ni/Co-rich oxides which induce crack closure.

(2) The complete oxidation induced crack closure effects can be quantitatively evaluated based on the simplified assumptions and the thickness of oxides measured using SEM. Significant reduction in ΔK is induced by the thick external oxides, which should be the primary factor causing the fatigue crack arrest.

(3) X-ray CT is capable to capture the morphology of the oxidized fatigue crack in three dimensions. Crack opening displacement (COD) measured using the segmented crack could be used to assess the crack closure effects induced by oxidation. It should be noted the COD data is overestimated in the situation of significant oxidation intrusion, such as the test at 1-90-1-1 frequency.

(4) The partial oxidation induced crack closure effect is evaluated based on the model of Suresh and Louat et. al as well as by evaluating the COD data from X-ray CT for the 1-1-1-1 frequency test. An obvious reduction in ΔK results from the oxides formed close to the crack tip and is confirmed by both models, though the degree of reduction in ΔK is different according to the two models.

(5) The carbides located at the inter-dendritic regions significantly deflect the fatigue crack path for L sample in the pre-cracking stage. Subsequently, the roughness-induced and oxidation-induced crack closure co-result in the crack arrest of L sample tested at 650 ℃ and 1-1-1-1 waveform.

Appendix A Detailed Precrack Process and Crack Length Calibrations

ΔK of 20 MPa√m was firstly applied to initiate the crack growth from the notch. As the crack grew, the ΔK would of course increase if tested under the same load conditions. To keep the ΔK constant within any given testing step, the load range (ΔP) is therefore adjusted whenever the X/Y PD ratio increased by 0.1 (approximately corresponding to a crack growth of 80 to 100 μm), this leads to a variation of no more than 2% in applied ΔK values. Hence the ΔK level is maintained to within ±2% during a constant ΔK testing step. At each ΔK step, the crack grew through four times the monotonic plastic zone size to obtain consistent crack growth behaviour and avoid overload effects on subsequent crack growth at lower ΔK levels. For instance, at a ΔK = 20 MPa√m the maximum ΔK experienced would be 20.4 MPa√m, which is unlikely to impose any overload effects on this high-strength material. After the crack grew

through the four monotonic plastic zone sizes, the load range is adjusted again to achieve a ΔK level stepped down by 10%. Fig. 14 below shows the load history for the precrack.

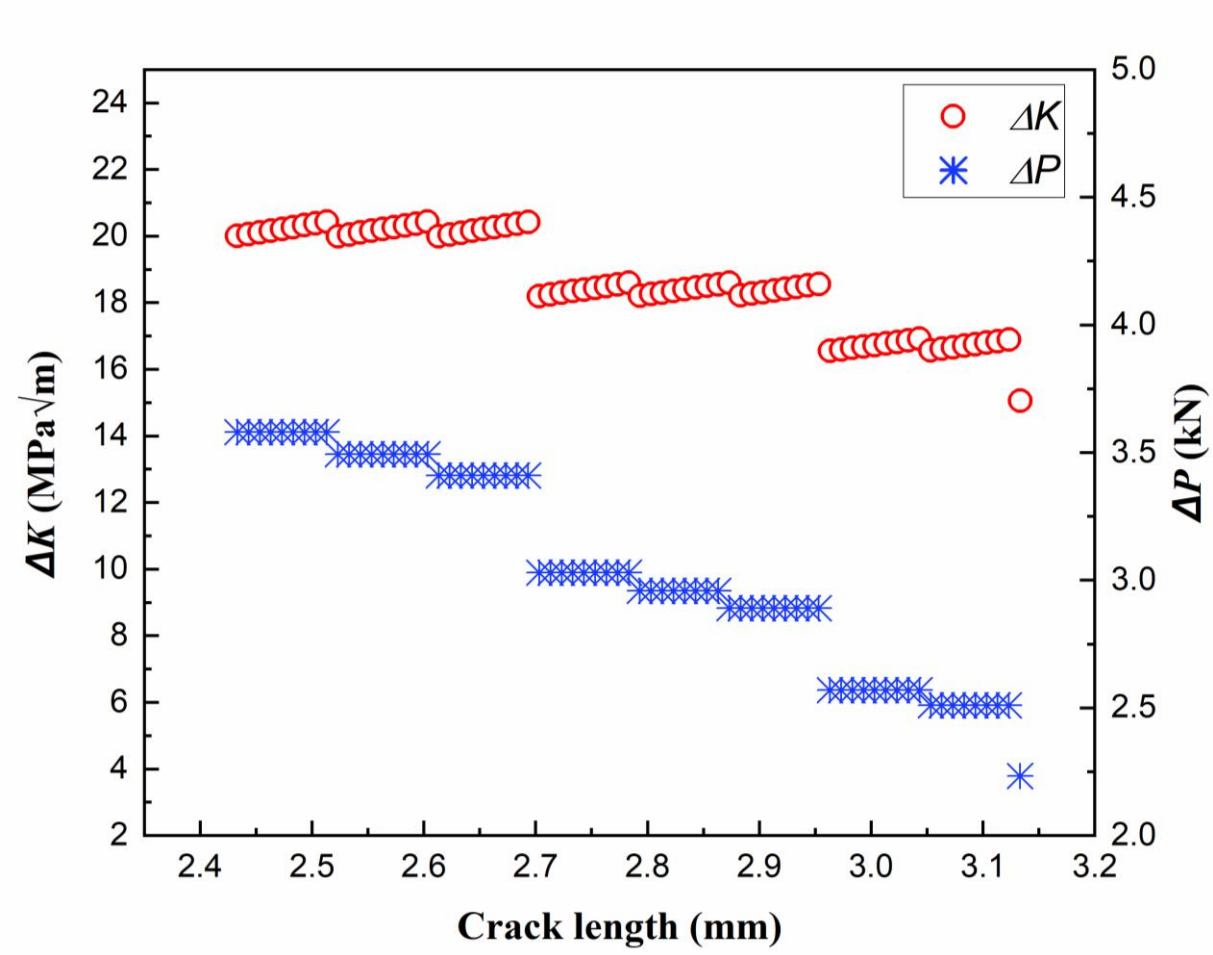

Fig. 14 Applied ΔK and ΔP against the crack length, showing the load control used to maintain ΔK to within ±2%

The PD calibration curve is obtained empirically and checked against each test, the fit used is cubic fitting. The original PD calibration is obtained at room temperature from data obtained on previous studies on a geometrically similar large scale 2D sample, where a lengthening slot is introduced and carefully measured, while the variation in PD with increased crack length was noted. Post-test fracture surface observations between the average benchmark depths on fracture surface at known numbers of cycles and the crack length predicted from the empirical PD calibration has been performed at high temperatures (725 ℃, 650 ℃, 550 ℃, 450 ℃). Typically, the deviation in measured and PD inferred crack length is reasonable, less than 4%. Secondly, all the parameters, such as compliance (Y), stress intensity (ΔK) and da/dN are recalculated based on the actual measured crack length. Specific methods for the recalibration can be found in: 'http://eprints.soton.ac.uk/id/eprint/420749.'

A stabilized power supply is used throughout – Matelect DCM-2 DCPD Crack Growth Monitor. However, there is still a problem associated with thermo-electrical effects, lack of stability in supplying current and change of temperature (at room temperature, the issue does

not arise). Relevant background information can be found in 'ASTM E647 - 13e1 Standard Test Method for Measurement of Fatigue Crack Growth Rates, n.d.' To reduce the noise coming from the temperature effects, reference probes are required, followed by a series of smoothing methods, which can be found in the appendix of the PhD thesis: 'Oxidation-fatigue mechanisms at moderate service temperatures in single crystal turbine blade materials.' 'http://eprints.soton.ac.uk/id/eprint/420749.'

Acknowledgement

The authors would like to thank the EPSRC (Grant no:EP/M000710/1) for funding support, the China Scholarship Council, China, for financial support, Dr. Gordon McColvin at GE Power for providing the materials and Dr. Katy Rankin at μ-VIS X-ray Imaging Center of University of Southampton for the X-ray CT characterization.

Data availability

Supporting data is available from the University of Southampton Institutional repository on request from (added upon publication).

Reference

[1] C.T. Sims, A contemporary view of nickel-base superalloys, JOM 18(10) (1966) 1119-1130.
[2] R.C. Reed, The superalloys: fundamentals and applications, Cambridge university press2008.
[3] J.C. Stinville, E. Martin, M. Karadge, S. Ismonov, M. Soare, T. Hanlon, S. Sundaram, M.P. Echlin, P.G. Callahan, W.C. Lenthe, V.M. Miller, J. Miao, A.E. Wessman, R. Finlay, A. Loghin, J. Marte, T.M. Pollock, Fatigue deformation in a polycrystalline nickel base superalloy at intermediate and high temperature: Competing failure modes, Acta Materialia 152 (2018) 16-33.
[4] A. Sato, Y.L. Chiu, R.C. Reed, Oxidation of nickel-based single-crystal superalloys for industrial gas turbine applications, Acta Materialia 59(1) (2011) 225-240.
[5] H.Y. Li, J.F. Sun, M.C. Hardy, H.E. Evans, S.J. Williams, T.J.A. Doel, P. Bowen, Effects of microstructure on high temperature dwell fatigue crack growth in a coarse grain PM nickel based superalloy, Acta Materialia 90 (2015) 355-369.
[6] M.Y. He, A.G. Evans, A model for oxidation-assisted low cycle fatigue of superalloys, Acta Materialia 58(2) (2010) 583-591.
[7] A.G. Evans, M.Y. He, A. Suzuki, M. Gigliotti, B. Hazel, T.M. Pollock, A mechanism governing oxidation-assisted low-cycle fatigue of superalloys, Acta Materialia 57(10) (2009) 2969-2983.
[8] L. Viskari, M. Hörnqvist, K.L. Moore, Y. Cao, K. Stiller, Intergranular crack tip oxidation in a Ni-base superalloy, Acta Materialia 61(10) (2013) 3630-3639.
[9] A.A.N. Németh, D.J. Crudden, D.E.J. Armstrong, D.M. Collins, K. Li, A.J. Wilkinson, C.R.M. Grovenor, R.C. Reed, Environmentally-assisted grain boundary attack as a mechanism of embrittlement in a nickel-based superalloy, Acta Materialia 126 (2017) 361-371.
[10] H.E. Evans, H.Y. Li, P. Bowen, A mechanism for stress-aided grain boundary oxidation ahead of cracks, Scripta Materialia 69(2) (2013) 179-182.
[11] C.J. McMahon, L.F. Coffin, Mechanisms of damage and fracture in high-temperature, low-cycle fatigue of a cast nickel-based superalloy, Metallurgical Transactions 1(12) (1970) 3443-3450.
[12] L. Ma, K.-M. Chang, Identification of SAGBO-induced damage zone ahead of crack tip to characterize sustained loading crack growth in alloy 783, Scripta Materialia 48(9) (2003) 1271-1276.
[13] R.H. Bricknell, D.A. Woodford, Grain boundary embrittlement of the iron-base superalloy IN903A, Metallurgical Transactions A 12(9) (1981) 1673-1680.
[14] H.S. Kitaguchi, H.Y. Li, H.E. Evans, R.G. Ding, I.P. Jones, G. Baxter, P. Bowen, Oxidation ahead of a crack tip in an advanced Ni-based superalloy, Acta Materialia 61(6) (2013) 1968-1981.
[15] M. Hörnqvist, L. Viskari, K.L. Moore, K. Stiller, High-temperature crack growth in a Ni-base superalloy during sustained load, Materials Science and Engineering: A 609 (2014) 131-140.
[16] S. Suresh, G.F. Zamiski, D.R.O. Ritchie, Oxide-Induced Crack Closure: An Explanation for Near-Threshold Corrosion Fatigue Crack Growth Behavior, Metallurgical and Materials Transactions A 12(8) (1981) 1435-1443.
[17] A.T. Stewart, The influence of environment and stress ratio on fatigue crack growth at near threshold stress intensities in low-alloy steels, Engineering Fracture Mechanics 13(3) (1980) 463-478.
[18] P.K. Liaw, T.R. Leax, R.S. Williams, M.G. Peck, Influence of oxide-induced crack closure on near-threshold fatigue crack growth behavior, Acta Metallurgica 30(12) (1982) 2071-2078.
[19] P. Paris, R. Bucci, E. Wessel, W. Clark, T. Mager, Extensive study of low fatigue crack growth rates in A533 and A508 steels, ASTM STP 513 (1972) 141-176.
[20] J.M. Martínez-Esnaola, A. Martín-Meizoso, E.E. Affeldt, A. Bennett, M. Fuentes, HIGH TEMPERATURE FATIGUE IN SINGLE CRYSTAL SUPERALLOYS, Fatigue & Fracture of Engineering Materials & Structures 20(5) (1997) 771-788.
[21] N. Louat, K. Sadananda, M. Duesbery, A.K. Vasudevan, A Theoretical Evaluation of Crack Closure, Metallurgical and Materials Transactions A 24(10) (1993) 2225-2232.
[22] Y.G. Tan, D.J. Bull, R. Jiang, A. Evangelou, S. Chaudhuri, S. Octaviani, F. Pierron, N. Gao, H. Toda, I. Sinclair, P.A.S. Reed, Data rich imaging approaches assessing fatigue crack initiation and early propagation in a DS superalloy at room temperature, Materials Science and Engineering: A 805 (2021) 140592.
[23] H. Toda, I. Sinclair, J.Y. Buffière, E. Maire, T. Connolley, M. Joyce, K.H. Khor, P. Gregson, Assessment of the fatigue crack closure phenomenon in damage-tolerant aluminium alloy by in-situ

high-resolution synchrotron X-ray microtomography, Philosophical Magazine 83(21) (2003) 2429-2448.
[24] H. Toda, I. Sinclair, J.Y. Buffière, E. Maire, K.H. Khor, P. Gregson, T. Kobayashi, A 3D measurement procedure for internal local crack driving forces via synchrotron X-ray microtomography, Acta Materialia 52(5) (2004) 1305-1317.
[25] R. Jiang, D.J. Bull, D. Proprentner, B. Shollock, P.A.S. Reed, Effects of oxygen-related damage on dwell-fatigue crack propagation in a P/M Ni-based superalloy: From 2D to 3D assessment, International Journal of Fatigue 99 (2017) 175-186.
[26] A. Evangelou, K.A. Soady, S. Lockyer, N. Gao, P.A.S. Reed, On the mechanism of oxidation-fatigue damage at intermediate temperatures in a single crystal Ni-based superalloy, Materials Science and Engineering: A 742 (2019) 648-661.
[27] L. Ma, K.-M. Chang, S.K. Mannan, Oxide-induced crack closure: an explanation for abnormal time-dependent fatigue crack propagation behavior in INCONEL alloy 783, Scripta Materialia 48(5) (2003) 583-588.
[28] X.-K. Zhu, J.A. Joyce, Review of fracture toughness (G, K, J, CTOD, CTOA) testing and standardization, Engineering Fracture Mechanics 85 (2012) 1-46.
[29] A.K. Vasudeven, K. Sadananda, N. Louat, A review of crack closure, fatigue crack threshold and related phenomena, Materials Science and Engineering: A 188(1) (1994) 1-22.
[30] A. Vasudevan, K. Sadananda, N. Louat, Reconsideration of fatigue crack closure, Scripta metallurgica et materialia 27(11) (1992) 1673-1678.
[31] C.F. Shih, Relationships between the J-integral and the crack opening displacement for stationary and extending cracks, Journal of the Mechanics and Physics of Solids 29(4) (1981) 305-326.
[32] I.O.f. Standardization, Metallic Materials: Fatigue Testing: Fatigue Crack Growth Method. ISO 12108, ISO2002.
[33] C.S. Wiesner, S.J. Maddox, W. Xu, G.A. Webster, F.M. Burdekin, R.M. Andrews, J.D. Harrison, Engineering critical analyses to BS 7910 — the UK guide on methods for assessing the acceptability of flaws in metallic structures, International Journal of Pressure Vessels and Piping 77(14) (2000) 883-893.
[34] Y. Gao, R.O. Ritchie, M. Kumar, R.K. Nalla, High-cycle fatigue of nickel-based superalloy ME3 at ambient and elevated temperatures: Role of grain-boundary engineering, Metallurgical and Materials Transactions A 36(12) (2005) 3325-3333.
[35] L. Garimella, P. Liaw, D. Klarstrom, Fatigue behavior in nickel-based superalloys: A literature review, Jom 49(7) (1997) 67-71.
[36] J.M. Schooling, M. Brown, P.A.S. Reed, An example of the use of neural computing techniques in materials science—the modelling of fatigue thresholds in Ni-base superalloys, Materials Science and Engineering: A 260(1) (1999) 222-239.
[37] S. Suresh, R.O. Ritchie, Some considerations on the modelling of oxide-induced fatigue crack closure using solutions for a rigid wedge inside a linear elastic crack, Scripta Metallurgica 17(4) (1983) 575-580.
[38] S. Suresh, Fatigue of Materials, 2 ed., Cambridge University Press, Cambridge, 1998.
[39] Z. Shan, Y. Leng, Analytical estimation of asperity-induced crack closure, Scripta Materialia 36(1) (1997) 137-143.
[40] R.J. Kashinga, L.G. Zhao, V.V. Silberschmidt, F. Farukh, N.C. Barnard, M.T. Whittaker, D. Proprentner, B. Shollock, G. McColvin, Low cycle fatigue of a directionally solidified nickel-based superalloy: Testing, characterisation and modelling, Materials Science and Engineering: A 708 (2017) 503-513.
[41] G.T. Gray, J.C. Williams, A.W. Thompson, Roughness-Induced Crack Closure: An Explanation for Microstructurally Sensitive Fatigue Crack Growth, Metallurgical Transactions A 14(2) (1983) 421-433.
[42] S. Suresh, R.O. Ritchie, A geometric model for fatigue crack closure induced by fracture surface roughness, Metallurgical Transactions A 13(9) (1982) 1627-1631.